Physical Variability in Meter-Scale Laboratory CO_2 Injections in Faulted Geometries

Malin Haugen[1] · Lluís Saló-Salgado[2,3] · Kristoffer Eikehaug[1] · Benyamine Benali[1] · Jakub W. Both[4] · Erlend Storvik[4] · Olav Folkvord[1] · Ruben Juanes[2,3] · Jan Martin Nordbotten[4,5] · Martin A. Fernø[1,5]

Abstract

Carbon, capture, and storage (CCS) is an important bridging technology to combat climate change in the transition toward net-zero. The FluidFlower concept has been developed to visualize and study CO_2 flow and storage mechanisms in sedimentary systems in a laboratory setting. Meter-scale multiphase flow in two geological geometries, including normal faults with and without smearing, is studied. The experimental protocols developed to provide key input parameters for numerical simulations are detailed, including an evaluation of operational parameters for the FluidFlower benchmark study. Variability in CO_2 migration patterns for two different geometries is quantified, both between 16 repeated laboratory runs and between history-matched models and a CO_2 injection experiment. The predicative capability of a history-matched model is then evaluated in a different geological setting.

✉ Malin Haugen
     malin.haugen@uib.no

1   Department of Physics and Technology, University of Bergen, Bergen, Norway

2   Department of Civil and Environmental Engineering, Massachusetts Institute of Technology, Cambridge, MA 02139, USA

3   Earth Resources Laboratory, Department of Earth, Atmospheric and Planetary Sciences, Massachusetts Institute of Technology, Cambridge, MA 02139, USA

4   Center for Modeling of Coupled Subsurface Dynamics, Department of Mathematics, University of Bergen, Bergen, Norway

5   Center for Sustainable Subsurface Resources, Norwegian Research Center, Postboks 22 Nygårdstangen, 5838 Bergen, Norway

1 Introduction

As the prices of renewable energy are decreasing, carbon, capture, utilization, and storage represent a bridging technology to combat climate change in the transition period toward net zero. Geological carbon sequestration (GCS) could contribute to the energy transition by tackling emissions from existing energy assets, providing solutions in some of the sectors where emissions are hardest to reduce (like cement production), supporting the rapid scaling up of low-emissions hydrogen production, and enabling some CO_2 to be removed from the atmosphere through bio-energy and direct air capture with GCS (IEA 2021).

Carbon sequestration is based on the principle that the injected CO_2 becomes less mobile over time by porous media trapping mechanisms, where the relative importance between the governing processes depends on the subsurface conditions. In situ visualization of CO_2 injection and the trapping mechanisms are valuable for understanding the fluid flow and migration patterns during geological CO_2 sequestration (GCS), and the authors believe it is also important for enhancing public understanding and acceptance about CO_2 storage and security. The laboratory experiments presented in this paper are relevant for geological carbon storage as the main mechanisms are sustained, including capillarity, dissolution, and convective mixing, and it represents a unique possibility to test our simulation skills, because in contrast to the subsurface, here we can compare predictions to observations.

The FluidFlower concept links GCS research and dissemination through experimental rigs constructed at University of Bergen (UiB) that enable meter-scale, multiphase, quasi-two-dimensional flow on complex, yet representative geological geometries. Intermediate scale quasi-2D laboratory experiments are widely used to study multiphase porous media flow, including gravity unstable flows in the presence of heterogeneity (Glass et al. 2000; Van De Ven and Mumford 2018, 2020; Krishnamurthy et al. 2022), and CO_2 migration and dissolution (Kneafsey and Pruess 2010; Trevisan et al. 2017; Rasmusson et al. 2017). These approaches enable visualizing and studying a range of porous media flow dynamics in engineered representative porous media using unconsolidated beads or sand grains. A key feature of the FluidFlower rigs is the ability to repeat experiments in the same geometry, without the need to remove the sands between repeated runs. Different geological geometries are constructed using unconsolidated sands, and simulation models based on the experimentally studied geometry provide key input parameters for numerical simulations. Gaseous and aqueous forms of CO_2 are distinguished with pH-sensitive dyes, and the multiphase fluid flow dynamics is captured with time-lapse imaging. The Darcy Scale Image Analysis toolbox (DarSIA, Nordbotten et al. 2023) is utilized to analyze the images to quantify key parameters and variability in the experimentally observed CO_2 migration patterns.

The goal of this study is twofold: First, evaluate and discuss physical reproducibility in repeated experimental CO_2 injections in two different geometries. Second, perform dedicated laboratory experiments for history matching to determine the predicative capability of the validated and physics-based model in a different geological setting using the same sands (Saló-Salgado et al. 2023). The paper is divided into three sections: (1) laboratory protocols for measurements of petrophysical sand properties and CO_2 injections, (2) main laboratory results are discussed, including physical variability between repeated CO_2 injections in two geological geometries, and (3) numerical modeling of experimental CO_2 injections with history matching and simulation with comparison to physical experiments.

2 Methods and Materials

2.1 Fluids

Fluid properties are summarized below (Table 1), and the porous media was initially fully saturated with an aqueous pH-indicator mix, referred to as "formation water". The CO_2 was injected as dry gas and will partially partition into the formation water to form "CO_2 saturated water". The image analysis (Section 1.6) can distinguish between the different phases from the added pH sensitive dyes (gas and aqueous phases are originally transparent). Three different pH-indicator mixes (Fig. 1) were used to test visual impact on tracking CO_2 gas migration (as absence of color) and CO_2 saturated water, and further how this is influenced by the image segmentation using DarSIA (Nordbotten et al. 2023).

The pH of the formation water impacts the equilibrium between gaseous CO_2 and the aqueous phase, and it was expected pH-indicator mix 3 (pH approximately 10) would lead to higher CO_2 dissolution rate (and less mobile gaseous CO_2) compared with mix 1 and 2 (pH approximately 8). The rate of dissolution impacts migration patterns for both gaseous CO_2 and CO_2 saturated water, and the CO_2 concentration in CO_2 saturated water also influence gravitational-dominated flow processes due to density differences. At standard conditions (20 °C and 1013 millibar), the maximum solubility of CO_2 in water is about 1.7 g of CO_2 pr kg of water (The Engineering ToolBox 2008), corresponding to an increase in density of around 1–2%.

2.2 Physical Properties of the Quartz Sand—Experimental Protocol

When sediments (particles) accumulate they form sedimentary deposits which compose layers of rock. Within a deposit, the individual particles vary in size, shape, etc., and hence, the layer they constitute has certain macroscopic properties such as porosity and permeability (Krumbein and Monk 1942). These mass properties will vary with, among others, the combination of properties of the particles and the conditions of packing (Krumbein and Monk 1942). The geologically important characteristics of sediments might be described using six measurable quantities: size, shape (sphericity), roundness (angularity), mineral composition, surface texture and orientation. The following sections describe the procedures to measure the properties of the unconsolidated sands.

2.2.1 Sand preparation

The unconsolidated quartz sand used was purchased from a commercial Norwegian supplier. Based on the stated and available grain size ranges, desired grain size ranges for this study were chosen according to the Wentworth scale (Wentworth 1922) (Table 2). The received sands were sieved prior to building the geological geometries to achieve increased control of the used grain size ranges. Dry wire-mesh sieves (*Glenammer*) staked on a mechanical shaker were used, before the sands were washed in a two-step process: (1) Rinsed with tap water to remove fine material, (2) Acid washed using HCl until carbonate impurities were dissolved, and no more CO_2 bubbles were observed (varying from 24 to 72 h for the different sand types). The acid was then neutralized, and the sand was rinsed with tap water. After washing, the sands were dried at 60 °C

Table 1 Fluids and pH-indicator mixes with their expected pH values

Fluid (phase)	Composition	pH	Usage
Deionized water	H_2O	–	Petrophysical sand properties
Acid (aq)	Tap water with - Above 0.1 M hydrochloric acid (HCl)	<2 *	Remove carbonate impurities during sand cleaning
pH-indicator mix 1 (aq)	Deionized water with - 0.14 mM bromothymol blue (BTB⁻) - 0.43 mM methyl red (Mre⁻) - 0.10 mM hydroxide (OH⁻) - 0.67 mM sodium ions (Na⁺)	~8.3	Initial formation fluid to enable detecting CO_2 dissolution in the aqueous phase
pH-indicator mix 2 (aq)	Deionized water with - 0.14 mM bromothymol blue (BTB⁻) - 0.10 mM hydroxide (OH⁻) - 0.24 mM sodium ions (Na⁺)	~8.3	Initial formation fluid to enable detecting CO_2 dissolution in the aqueous phase
pH-indicator mix 3 (aq)	Deionized water with - 0.75 mM bromothymol blue (BTB⁻) - 1.00 mM hydroxide (OH⁻) - 0.67 mM sodium ions (Na⁺)	<10.4**	Initial formation fluid to enable detecting CO_2 dissolution in the aqueous phase
CO_2 (g)	99.999%—5.0 purity	–	Injected as gaseous phase
Lye solution (aq)	Deionized water with 0.48 mM sodium hydroxide (NaOH)	<10.7**	Reset/clean the system after experiments (flush out CO_2 saturated water and trapped free gas)

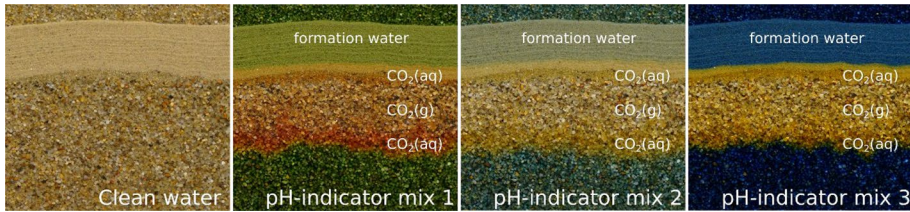*Maintained below pH 2 until stable. **Depending on exposure to air

Fig. 1 Illustration of different pH-indicator mixes used in the experiments, and their colored response to gaseous and dissolved CO$_2$ as supposed to the formation water. From left to right: Image of a layered sand formation saturated with clean water; same formation but saturated with pH-indicator mixes 1–3 in the presence of CO$_2$

Table 2 Desired grain-size range of sand used in this study and size of wire-mesh sieves used

Sand ID	Desired grain size range[a] [mm]	Desired grain size range[a] [phi scale]	Grade[a]
ESF	0.13 to 0.36[b]	2.9 to 1.5	Fine sand
C	0.5 to 0.71	1.0 to 0.5	Coarse sand (lower)
D	0.71 to 1.0	0.5 to 0.0	Coarse sand (upper)
E	1.0 to 1.41	0 to -0.5	Very coarse sand (lower)
F	1.41 to 2.0	−0.5 to −1.0	Very coarse sand (upper)
G	2.0 to 2.8	−1.0 to −1.5	Granule gravel

[a]Sieved range and grade according to Wentworth class (Wentworth, C.K., 1922)

[b]Size range provided by supplier. Sand ESF was not sieved, only washed and dried to maintain fine particles

for at least 24 h and stored in clean 15 L plastic containers until use. Sands named ESF, C, E and F were used to build the geometries investigated here (Sect. 2.3), whereas all sand types were used in FluidFlower benchmark geometry (Fernø et al. 2023).

2.2.2 Protocol for petrophysical measurements

The petrophysical properties porosity (φ), absolute permeability (K) and endpoint relative permeability (kr) of the unconsolidated sand were measured using a sand column (Fig. 2). Custom-made end pieces (polyoxymethylene) with a Y-shaped passage enabled absolute pressure measurement (ESI, GSD4200-USB, −1 to 2.5 bara) at each end face, with milling for a round metal mesh and paper filter against the sand to maintain sand column integrity. A differential pressure transducer (Aplisens PRE-28, 0–2.5 bara) was positioned 154 mm from the top and bottom of the tube and measured the differential pressure across a 171 mm section of the sand column. The procedural steps for the petrophysical measurements are detailed below, and different fluids were injected through the sand column throughout the procedure. Note that all bottles and outlets were at the same height to ensure a stable system with no flow in or out of the sand column when fluid injection was stopped. Tubes were fixed in place to mitigate influence on measured sand column weight and produced fluids during endpoint relative permeability measurements.
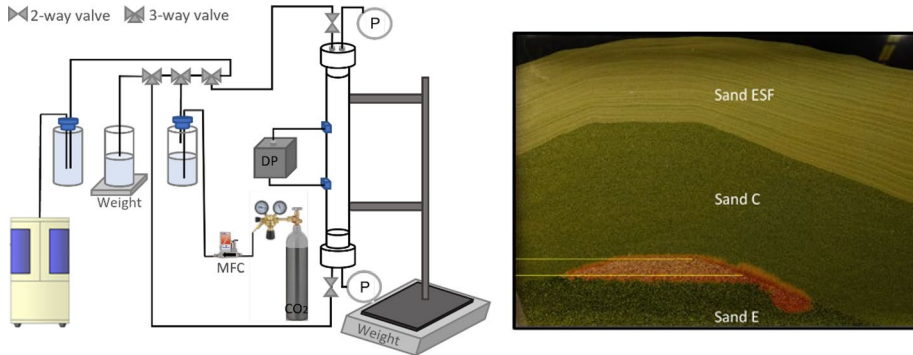
Fig. 2 Left: schematic of the experimental set-up used for measuring porosity, absolute permeability, and relative permeability (Sect. 2.2.3–2.2.5). A vertical Plexiglas tube (length 478.0 mm and diameter 25.8 mm) with metal mesh and 0.2 μm paper filter against the sand maintained sand column integrity. ESI pressure transducers (−1–2.5 bara) monitored inlet and outlet pressure and temperature. An Aplisens differential pressure transducer (0–2.5 bara) recorded the differential pressure in the middle of the sand column. Quizix QX pump controlled the volumetric rate of injected aqueous phases, whereas a Bronkhorst El-Flow Prestige mass flow controller with a maximum rate of 10ml/min was used for the CO_2 injection. Right: Example geometry used for gas column breakthrough experiments to obtain capillary entry pressure (height of gas column, distance between horizontal yellow lines), here for sand C

2.2.3 Porosity (φ) measurement

Porosity was calculated for all sand types using the following procedure:

1. The vertical tube, with bottom end-piece and filter attached, was filled with degassed, deionized (DI) water to a predetermined and known water height.
2. Dry sand was poured into the water-filled tube and settled at the bottom. Approximately 20 mm sand was added each time, and the tube was gently tapped during sand settling. Sand was added until the sand column height reached the predetermined level.
3. Water was constantly removed from the top of the tube during sand settling and the volume of the extracted water was measured cumulatively.
4. Prior to attaching the top end-piece, the tube was filled with DI (to minimize air between the end-piece and the sand) and the filter placed on top of the sand. Tubing attached to the end-piece was loosened to enable the displaced water to escape as the end-piece was placed into the tube without asserting force to the sand.

The extracted water volume in step 3 equals the sand grain volume, and the porosity was calculated from the ratio of the pore volume (bulk volume—grain volume) to bulk volume.

2.2.4 Absolute permeability (K) measurement

Absolute permeability was measured after the porosity measurement described above with the following procedure:

1. Degassed DI water was injected from the bottom with a high volumetric injection rate (650 ml/h for 3 h) to remove trapped gas bubbles, if any.
2. Flow direction was reversed (top endpiece used as inlet) and degassed DI water was injected using 5 ascending and descending constant volumetric injection rates between 200 and 600 ml/h, with 100 ml/h increments for 10 min. (Stable differential pressures were achieved.)
3. Differential pressures versus injection rate were recorded and used for calculation of absolute permeability using Darcy's law and is given by $Q = -K \cdot A \cdot \left(\frac{\Delta P}{L} \right)$, where Q is the flow rate, K is the absolute permeability, A is the cross-sectional area, ΔP is the differential pressure, and L is the unit length.

2.2.5 *Unsteady-state endpoint relative permeability (k_r) measurements*

The unsteady-state end-point relative permeabilities during both drainage and imbibition used CO_2-saturated water and CO_2. The average sand column end-point fluid saturation was calculated from volumetric and weight measurements. The following procedure was followed:

1. After absolute permeability measurements (Sect. 2.2.4), degassed DI water was miscibly displaced with CO_2-saturated DI water. This step was performed to avoid dissolution of gaseous CO_2 gas in the water phase during drainage CO_2 injection.
2. End-point drainage: CO_2 gas was injected from the top with a constant rate of 10 ml$_s$/min (10 ml/min @ standard conditions: 20 °C + 1013 millibar). The absolute inlet and outlet pressure (sands E, F, G) or differential pressure (sands ESF, C, D), were recorded during drainage. Water production was monitored during drainage (by weight), and CO_2 was injected until no further water production was recorded. The weight of the partially water saturated sand column was recorded. Endpoint relative permeability to CO_2 was calculated based on the pressure differential between 10 and 0 ml/min.
3. End-point imbibition: After the drainage process was completed, the injection was switched back to CO_2 saturated water and ramped up to a constant volumetric rate of 600 ml/h, also injected from the top. The pressures and weight of sand column were recorded during injection. When no additional gas was produced for 60 min, the final sand column weight was recorded and an injection cycle to measure water endpoint permeability was conducted.

2.2.6 Capillary Entry Pressure Measurement

The capillary entry pressure to gas was experimentally measured for each sand type based on observed gas column break-through experiments in the FluidFlower rig (Fig. 3). Different geometries were investigated, including anticlines with an "inverse V shape" top to an "inverse U shape" top, constructed using the sedimentary protocol detailed in Sect. 1.5. The porous media was saturated with pH-indicator mix 1 (see Table 1), and gaseous CO_2 was injected at 10 ml$_s$/min (10 ml/min @ standard conditions: 20 °C and 1013 millibar). The gas accumulation and column height were monitored with time-lapsed imaging to detect the maximum gas column height between the different sand layers and under the sealing layer (ESF). The observed gas column height (in meter) was converted to pressure to provide the entry pressure for each sand type, by: $P_C = \rho \cdot g \cdot h$, where P_C is the
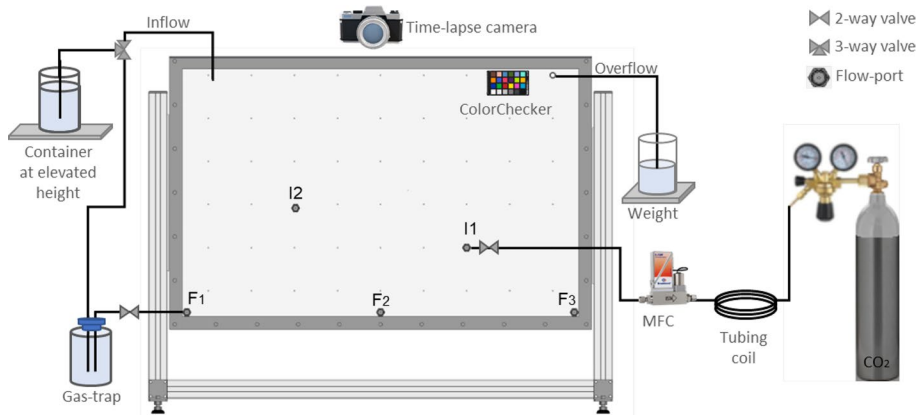
Fig. 3 Schematic overview of a tabletop FluidFlower (920×575 mm visible width x height within the frame) and the associated equipment. Liquids are injected through gravity (container at elevated height) or using a pump. During flushing and resetting the flow-cell, the flush-ports (F1–F3) are utilized, and as a preventive measure to avoid unwanted air bubbles trapped in tubing to enter the rig, a gas-trap was included. For gas injection (through port I1 or I2), the set-up consists of a CO_2 calibrated mass flow controller (MFC), CO_2 tank with regulator and a coil of tubing mitigate pressure fluctuations caused by the gas regulator. Inflow (tubing end) and outflow (always-open port) provide a constant hydraulic head and provide information about volume displaced if logged. A camera with time lapse function is used to acquire high-resolution images of the dynamics, and the ColorChecker ensure correction of colors during image analysis to mitigate changes in illumination. All flow ports are 1/8-inch NPT to 1/8 Swagelok, with inner diameter of 1.8 mm

capillary pressure, ρ is the density of the non-wetting phase, and h is the height of the non-wetting phase column.

2.3 Laboratory Injections of Carbon Dioxide

The FluidFlower enables engineering of meter-scale geological geometries using unconsolidated sands, and its design allows for repeated injections to evaluate reproducibility without removing the sand and rebuilding the geometry. The porous media was constructed using unconsolidated sands and held in place by two optically transparent panels in the front and the back, glued together to an aluminum frame with spacing of 10 mm. The flow cell has no-flow boundaries in the bottom and sides, whereas the top is open and in contact with atmospheric pressure. The size (920×575 mm visible width$\times$height) and design of the tabletop rig allow evaluate physical reproducibility between operationally identical experiments, and rapid testing of key operational conditions, e.g., different pH-indicator mixes, injection protocols, constructing different geological structures and the effect of degassed aqueous phase. Technical and mechanical properties of the FluidFlower rigs are detailed in Eikehaug et al. 2023.

Two different geometries (termed 'Albus' and 'Bilbo') were studied in this work (see Sect. 2.3). The experimental set-up consists of throttle valve and Swagelok valves (2- and 3-way), mass flow controller (MFC) (EL-FLOW Prestige FG-201CV 0–10 mls/min, BronkHorst) calibrated for CO_2, pressurized CO_2 canister including pressure regulator, gas trap, ColorChecker (X-Rite), and camera with time-lapse function (Albus geometry: Sony ZV-1, 5472×3080 pixels; Bilbo geometry: Sony A7III, lens SAMYANG AF 45 mm F1.8,

7952×4472 pixels). The high-resolution images enable monitoring and analysis of multiphase flow dynamics with single grain identification and are one of the main measurements in this set-up.

2.4 Fluid Injection Protocols and Initial Conditions

The protocol to prepare for CO_2 injection experiments used the following steps, with reference to Fig. 3:

1. Inject the preferred pH-indicator mix according to the experimental protocol, using the three injection ports (F1–F3) along the bottom of the rig.
2. Initiate inflow with open overflow port to ensure constant hydrostatic pressure during the experiment.
3. Bleed tubing/valves for CO_2 injection with fluid from the rig (and collect samples for pH measurements). Stabilize overflow before continuing.
4. Run a warm-up MFC sequence (100% open valve for 30 min) to reduce rate fluctuations.
5. At a low CO_2 injection rate, connect tubing to valve and let it pressurize according to protocol before the valve is opened.

   a. Some backflow of pH-indicator is expected; record time when the injected CO_2 displace the backflow fluid into the valve.
   b. Continue CO_2 injection as described in the protocol (Table 3).
   c. Log inflow and outflow rate (mass per timestep) to determine displaced volume.

6. Inject degassed lye solution to reset the fluids in the porous media.

We note that gas injection should follow a scripted MFC protocol, with sufficiently high injection rate to maintain gaseous CO_2 in the injection point. All experiments utilize two ports for CO_2 injection (except experiments AC06 and AC07 that used one port) at room temperature (approximately 23 °C) and atmospheric pressure at the free water table at the top of the rig (cf. Table 4). Temperature fluctuations were minimized, but not eliminated, in the laboratory space, and added some uncertainty.

Table 3 Condensed CO_2 injection protocol used in geometry Albus and geometry Bilbo. Comprehensive protocol found in SI. Table 1. I1 and I2 refer to injection in flow port 1 and port 2, respectively (Fig. 3)

Objective	Albus geometry		Bilbo geometry	
	Rate [ml$_s$/min][a]	Duration [hh:mm:ss]	Rate [ml$_s$/min][a]	Duration [hh:mm:ss]
I1 rate ramp-up	0.1–1.5	00:05:00	1.0–1.5	00:02:00
I1 injection	**2.0**	**00:45:00**	**2.0**	**01:03:13**
I1 rate ramp-down	1.5–0.1	00:05:00	1.5–0.5	00:03:00
I2 rate ramp-up	0.1–1.5	00:05:00	1.0–1.5	00:02:00
I2 injection	**2.0**	**01:15:00**	**2.0**	**01:12:52**
I2 rate ramp-down	1.5–0.1	00:04:42	1.5–0.5	00:03:00

[a]CO_2 injection rate in ml$_s$/min @ standard conditions: 20 °C and 1013 millibar

Table 4 Initial conditions for CO_2 injection experiments in the Albus (AC) and Bilbo (BC) geometries

Experiment	pH-indicator mix[a]	CO_2 inj. 1st/2nd port [g]	P [mbar][b] 48 h avg. $\pm\sigma$	CO_2 inj. Started	State of formation water degassing
AC02	1	0.179/0.283	999 ± 5	Oct 13th, 2021	Insufficient
AC03	1	0.176/0.283	994 ± 12	Oct 18th, 2021	Insufficient
AC04	1	0.176/0.283	996 ± 11	Oct 21st, 2021	Insufficient
AC05	1	0.176/0.283	995 ± 2	Oct 26th, 2021	Insufficient
AC06	1	0.459/0	989 ± 3	Oct 29th, 2021	Insufficient
AC07	1	0.981/0	993 ± 2	Dec 7th, 2021	Insufficient
AC08	1	0.176/0.284	1015 ± 2	Apr 21st, 2022	Insufficient
AC09	2	0.176/0.284	1010 ± 2	May 3rd, 2022	Insufficient
AC10	3	0.176/0.284	1018 ± 6	May 6th, 2022	Sufficient
AC14	1	0.176/0.284	1003 ± 1	Jun 10th, 2022	Sufficient
AC19	3	0.176/ 0.284	1020 ± 3	Oct 18th, 2022	Sufficient
AC22	3	0.176/ 0.284	1000 ± 1	Nov 15th, 2022	Sufficient
BC01	1	0.240/0.275	1020 ± 4	May 7th, 2022	Sufficient
BC02	1	0.240/0.275	992 ± 3	May 23rd, 2022	Sufficient
BC03	2	0.240/0.275	1006 ± 2	Aug 17th, 2022	Sufficient
BC04	3	0.240/0.275	1019 ± 3	Aug 31st, 2022	Sufficient

[a]Ref Table 4

[b]Atmospheric pressure from metrological data in Bergen (Norway) during each cycle (SI. Figure 4) (Geophysical Institute, 2022)

2.5 Procedure for Constructing Geometries

The size and operational capabilities of the tabletop FluidFlower make it a valuable asset to test and develop procedures and tools for constructing geometric features. A detailed sketch of the desired geological geometry is drawn on the front panel (Fig. 4), and dry sand with predetermined grain size is poured from the top into the water-filled flow cell.
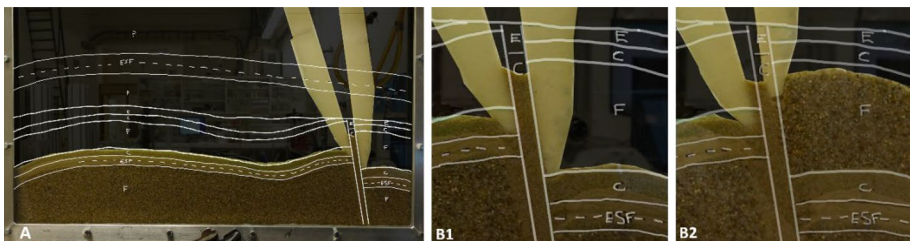

Fig. 4 Example of how to build features using unconsolidated sand. **A** The geological geometry is sketched on the transparent front panel. In this example the sand outside the fault was different from inside the fault, and two "angle-tools" (observed as off-white structures in the image series) separate the sands. **B** Details from fault construction. The fault and adjacent facies are deposited in a layer-by-layer approach for each sand type to match planned geometry. B1 show sand C added into the fault zone before sand F is added on the right (B2). The angle tool represents the boundary of the fault, and the sand to the right of the fault replaces the angle tool as it is lifted to maintain the sand within the fault

Hence, the geometry is built from bottom to top, and excess water is produced through the "overflow" port (cf. Figure 3) to maintain a constant water level during construction. For improved control during geometry building, the grain sizes in adjacent layers should be comparable in size to reduce mixing of grains. Increased complexity may be achieved by (1) increasing the number of sand types and creating sequences with many layers (i.e., each layer consists of one sand type), or (2) adding features such as faults or heterogeneities with different properties.

In this work, three tools were designed to construct a fault using unconsolidated sand:

– 'Angle tools' for sharp edges/faults made from pre-cut polycarbonate covered with polyester fiber mats. The fiber mats compress when inserted and "self-hold" to separate settling sand on either side.
– Pipette filler bulb attached to a steel pipe to smooth layered surfaces with gentle water puffs.
– A large diameter stiff tubing with a funnel on top for accurate direction of the sand.

2.6 Image Acquisition and Analysis

2.6.1 Camera Settings

Because the two geometries were operated in parallel in two FluidFlower rigs, two different cameras were used. For the Albus geometry the camera (Sony ZV-1) used the following settings: exposure time ¼ sec, F number 2.5, ISO 200, and manual focus. Standard light conditions were used to illuminate the rig, and light fluctuations were accounted for in the image analysis. Ideally, controlled light settings should be applied (Eikehaug et al. 2023). The camera was positioned in front of the rig. Images were captured at 5472×3080 pixels every 20 or 30 s during CO$_2$ injection, and every 300 s afterward until 48 h after CO$_2$ injection was initiated. While for the Bilbo geometry, the camera (Sony A7III, lens SAMYANG AF 45 mm F1.8) used the following settings: exposure time 1/6 s, F number 2.2, ISO 100, and manual focus. Images were captured at 7952×4472 pixels every 30 s during CO$_2$ injection and every 300 s afterward until the end of the experiment at 48 h.

Because of the image interval used to capture dynamics during each experiment, the full dataset consists of ~4800 images for each experiment. A subset that captures most of the flow dynamics was generated and used for the analysis presented here. These subsets consist of 214 images with the following intervals: 10 images prior to CO$_2$ injection start, images every 5 min during the first 360 min (6 h), images every 10 min from 360 min until 1440 min (24 h), and images every 60 min from 1440 min until end of experiment at 2880 min (48 h).

2.6.2 Phase Segmentation Through Image Analysis

The high-resolution images, acquired as described above, allow for a detailed visual examination of the fluid displacement along the front panel; fluid flow inside the reservoir remains unnoticed, yet the low depth of the geometry suggests relatively small deviations averaged over time. Micro-scale features such as gas bubbles or sand grain motion as well as macro-scale features as the phase segmentation of the CO$_2$-water mixture into the phases of water, CO$_2$ saturated water, and CO$_2$ gas can be identified from the photographs. The latter is possible due to the use of pH sensitive dyes. To analyze

the large and varying dataset for all experiments, the image analysis toolbox DarSIA (Nordbotten et al. 2023) is used. Altogether, the combination of photographs and image analysis software constitutes one of the main measurement instruments used in this work.

Prior to any analysis, DarSIA is used to unify the environment including the aligning of images and restricting to a fixed region of interest, normalizing temporal color and illumination fluctuations, as well as monitoring and correcting for small sand settling events. Having a cleaned representation of each image allows for comparing it to a fixed baseline image and therefore tracking advancing fluids as differences to the baseline.

A range of assumptions was made to quantitatively describe the multiphase flow from the FluidFlower rig, and a summary is included below:

    I.   we assume that gas-filled regions are 100% saturated with the gas (CO_2)
    II.   we assume a constant CO_2 concentration in the CO_2 saturated water
    III.   we do not account for the dynamics of the gas partitioning in the gas accumulation
    IV.   we can accurately calculate the volume of CO_2 injected during each run
    V.   we have accurate information about porosity and depth

Based on these assumptions, a tertiary phase segmentation of the images, identifying the formation water, dissolved CO_2 and mobile CO_2 phases, also locates the presence of all CO_2 within the geometry. The algorithmic phase segmentation boils down to thresholding both in terms of color and signal intensity. Depending on the pH-indicator used, two suitable monochromatic color channels are picked aiming at identifying first all CO_2 within the water, and then the gaseous CO_2 within all CO_2. Each sand type, saturated or unsaturated, reflects light differently. Thus, the thresholding algorithm is designed to take into account the heterogeneous nature of the geometry. It automatically dissects the analysis into sub-analyses of the different sand layers including choosing dynamic thresholding parameters for the different phases and layers. With this, an accurate segmentation of CO_2 and water is possible. The detection of gaseous CO_2 occurs on the Darcy scale. It should be emphasized that this possibly leads to ignoring single gas bubbles while at other times enlarging them due to the averaging procedure and specific choice of thresholding parameters, used for converting the fine scale images to coarse scale data. On the larger scale, this effect is noticeable but plays only a minor role. The segmentation and its accuracy are illustrated in Fig. 5.
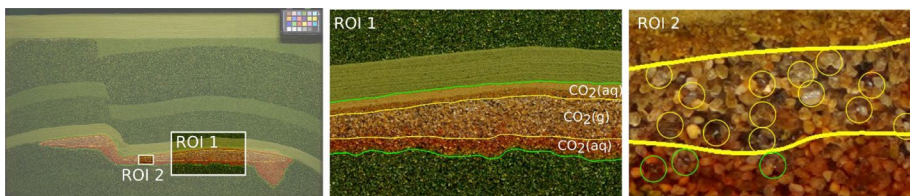

Fig. 5 Left: Illustration of the phase segmentation for BC01 after one hour of CO_2 injection. Center (ROI1): Segmentation with the transition zones of mobile to dissolved CO_2 as well as from dissolved CO_2 to water being entirely associated to the mobile and dissolved CO_2 phases, respectively. Right (ROI2): Highlighted, manually detected gas bubbles associated to dissolved (green circles) and mobile (yellow circles) CO_2 phases, illustrating the accuracy of the segmentation algorithm

3 Results and Discussion

3.1 Textural Sand Properties

The most important textural properties of natural clastic sediments can be expressed as five quantities: (1) grain size, (2) sorting, (3) sphericity, (4) roundness (angularity), and (5) packing (Beard and Weyl 1973). The grain size and sorting are measurable, and important factors in the porosity and permeability, however, packing (grain arrangement) of unconsolidated sand is difficult to measure and to assess its impact on porosity and permeability (Beard and Weyl 1973). Key sand grain properties were derived from segmented, binary microscopic images (Zeiss, Axio Zoom.V16) to obtain the distributions of sand grain width, length, and sphericity using Python and OpenCV functions (see Table 5). The grain size (mm) was converted to phi scale, where (*grain size*) $_{in\ phi}$ = -log_2 * (*grain size*) $_{in\ mm}$ (Krumbein 1936). The grain size measurements and sphericity demonstrate that many grains were noncircular, and each sand type had a larger distribution (SI. Fig. 1) than expected from the sieving process. According to Folk and Ward (1957), standard deviation (std) of grain size in phi-scale is a measure of sorting, and according to their classification, std of 0.71–1.00 (sand ESF) is moderately sorted, while 0.35–0.50 (sand G) is well sorted and < 0.35 (sand C, D, E and F) is very well sorted.

3.2 Petrophysical Properties

Measurements of the petrophysical properties were performed as detailed in Sect. 1.2, and the results are presented in Table 6. The petrophysical properties are used as input to simulation models for performing history match (Sect. 3) of the CO$_2$ injection experiments presented here, and in and associated numerical simulations (Saló-Salgado et al. 2023).

Comparing grain size versus sorting, sand ESF, C and D is within the range of grain sizes studied by Beard and Weyl 1973, and for wet-packed sand they observed that the porosity remained about the same regardless of grain size, which is the same as observed in the measured porosity presented here (Table 6). The permeability for unconsolidated sand varies with the square of an average diameter (Krumbein and Monk (1942), and references therein), and this is also the case for the measured values presented here (Table 6). Dataset from the literature is compared to the measured values in SI. Fig. 2. The capillary entry pressure was influenced by grain orientation and packing, and we observe differences between horizontal layers and vertical features (like a fault zone) in the studied geometries (see SI. Fig. 3). The sensitivity is used in the history matching of capillary entry pressures in the numerical modeling of the experimental CO$_2$ injections.

The inner diameter of the cylindrical tube used during permeability measurements should be minimum 8–10 times the maximum particle size of the tested sand column (Chapuis 2012). The geometric mean width and length for sand F and sand G (Table 5) are on this threshold value (8–10 times) with an inner tube diameter of 25.8 mm. Hence, this adds to the uncertainty to the measured permeability values as the relatively large grain size versus tube diameter may lead to poor packing conditions and preferential flow along tube walls (Chapuis 2012). We did not observe preferential flow paths along the walls in this work but note that our confidence in reported parameters for sands F and G is lower than other sands.

Table 5 Calculated properties of samples of the sieved sand, including width, length, and sphericity

Sand ID	# Grains analyzed	Grain size width		Grain length		Sphericity[a]	
		Geomean ± std [mm]	Mean phi scale ± std	Geomean ± std [mm]	Mean phi scale	Geomean	Std
ESF[b]	100	0.16 ± 0.12	2.62 ± 0.82	0.26 ± 0.17	1.94	–	–
C	1127	0.67 ± 0.09	0.58 ± 0.18	0.86 ± 0.17	0.21	0.69	0.10
D	1190	1.05 ± 0.14	−0.07 ± 0.19	1.36 ± 0.23	−0.45	0.68	0.11
E	1000	1.44 ± 0.17	−0.53 ± 0.17	1.87 ± 0.31	−0.90	0.64	0.14
F	1112	1.78 ± 0.26	−0.83 ± 0.22	2.25 ± 0.43	−1.17	0.59	0.18
G	959	2.56 ± 0.56	−1.35 ± 0.38	3.27 ± 0.70	−1.71	0.39	0.26

[a]Two-dimensional sphericity where circular = 1.0. Calculated as $(4 * \pi * Area)/(Circumference^2)$, where area and circumference are calculated using the OpenCV functions contourArea and arclength, respectively

[b]ESF grains were measured manually using a distance functionality in the Zeiss software because the grains were not possible to separate due to electrostatic forces

Table 6 Calculated porosity, absolute permeability, endpoint relative permeability for gas and water and capillary entry pressure for each sand

Sand ID	Porosity[a]	K [D][b]	Endpoint gas (CO$_2$)		Endpoint water		Capillary entry pressure
			S_{wi}	$k_{rel.gas}$	$1-S_g$	$k_{rel.water}$	Pc [mbar]
ESF	0.44	44	0.32	0.09	0.86	0.71	15.0
C	0.44	473	0.14	0.05	0.90	0.93	3.3
D	0.44	1110	0.12	0.02	0.92	0.95	0.9
E	0.45	2005	0.12	0.10	0.94	0.93	0.26[c]
F	0.44	4259	0.12	0.11	0.87	0.72	0.10[c]
G	0.45	9580	0.10	0.16	0.94	0.75	0.01[c]

[a]average based on constructing each sand pack twice with the same sand sample

[b]average calculated from one ascending and descending cycle (9 data points) for each sand

[c]calculated from the power function of the trendline in the log–log plot of Pc against geometric mean grain width for ESF, C and D sand because gas accumulation was not detectable during the capillary entry pressure measurements

3.3 Geological geometries

The geological geometries (Fig. 6) were motivated by the relationship between fluid flow and the presence of folds and faults in sedimentary rocks and basins. Two layered geometries with folds and faults with different properties (detailed below) were used to evaluate our ability to incorporate and investigate such geological features using unconsolidated sand, following three guiding principles: (1) enable realistic CO$_2$ flow pattern and trapping scenarios with increasing modeling complexity, (2) being sufficiently idealized so that the sand facies can be reproduced numerically with high accuracy, and (3) be able to operate, monitor and reset the fluids within a reasonable time frame.

Both geometries include two main reservoir sections separated by a lower seal (sand ESF) unit overlain by a regional sealing unit at the top of the geometry. For geometry Albus (Fig. 6, top), the layers are folded and have two anticlines, one toward the left edge of the rig and one to the right. The right anticline is offset by a listric normal fault, causing a discontinuity in the lower sealing unit. The fault is represented by a fault plane (~ 28 mm, sand C) with an 80 ° dip angle and lower permeability compared with the main reservoir (sand F). Features of the listric normal fault cause a rollover anticline on the footwall (right side of the fault), representing another structural trap. The upper reservoir section consists of layers of high permeability sand (*Upper F and E, and Middle F*) intersected by a layer of lower permeability sand (*Upper C*), and the lower reservoir section consists of uniform high permeability sand (*Lower F*). For geometry Bilbo (Fig. 6, bottom), one can imagine that there has been folding that created an anticline across the field of view, which later has been faulted. The structure has an erosional surface overlayed by a *Top Regional Sealing* unit (sand ESF). Note that the fault zone is not included, and the dip (70–80 degrees) and throw changes downwards in the reservoir layers. In contrast to geometry Albus, the *Lower Sealing* layer between the two reservoir sections in geometry Bilbo is continuous, and the sealing properties are therefore expected to be maintained. This could be described as smearing or drag folding and is a common feature when the clay content is high and is a feature which could have a
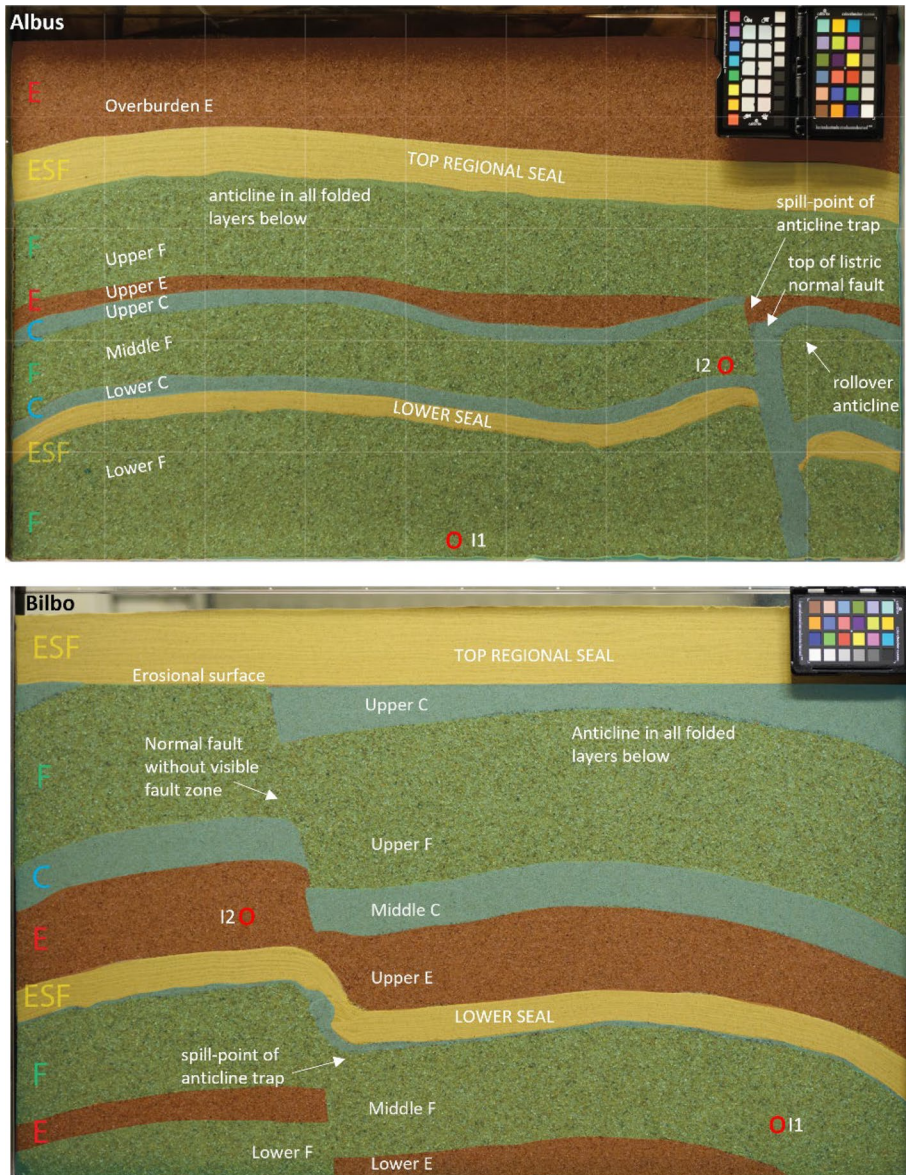
Fig. 6 The Albus (top) and Bilbo (bottom) geological geometries. Colors represent each sand type (red: sand E; green: sand F; yellow: sand ESF; blue: sand C) with grain size distributions and petrophysical properties listed in Table 2 and 5, respectively. A free water table of a few centimeters can be seen at the top of each geometry. Ports used for CO_2 injection are marked with red circles. Albus geological model is overlain with a 1000×1000 mm Cartesian grid with [0,0] in the lower left corner

large impact on fault transmissibility and fluid flow in the reservoir. Note that the drag/smear feature does not contain clay in geometry Bilbo, and because of increased leakage potential along the vertical no-flow boundaries, the layers dip downwards toward the edges to reduce this risk.

3.4 Image Analysis Sensitivity

The different pH-indicator mixes (Table 1) constitute the visual markers for the image analysis, and threshold parameters must be chosen to properly identify the different phases. As shown from Fig. 1, the responses of the different pH-indicators to the presence of CO_2 span different ranges of color variations. Comparing the chemically similar pH-indicator mixes 1 and 2, the first shows a larger span of colors than the latter. As a consequence of the latter, the thresholding algorithm is more sensitive with respect to the threshold parameters, resulting in systematic over-detection of the gaseous phase (Fig. 7). A similar conclusion can be drawn for the comparison of the chemically different pH-indicator mixes 1 and 3. Across the different experiments using the same pH-indicator mix, the same thresholding algorithms and parameters have been used. The calibration of the three sets of parameters was performed based on visual examination, without comparison across the mixes.

3.4.1 Mass Calculations

After an image is segmented into formation water, CO_2-saturated water and mobile CO_2, the total mass of each CO_2 phase can be determined. The total CO_2 mass $m_{CO_2}^{total}$ is known at any time, cf. injection profile in Table 3. Thus, assuming that all CO_2 in the rig either is mobile or dissolved, cf. assumption III, it is sufficient to determine the mass of mobile CO_2, $m_{CO_2}^{mobile}$, while the mass of dissolved CO_2 is given by $m_{CO_2}^{dissolved} = m_{CO_2}^{total} - m_{CO_2}^{mobile}$.

The mass of mobile CO_2, $m_{CO_2}^{mobile}$, is determined as pixel-wise sum of the pixel-wise defined mass density of mobile CO_2, $\rho_{CO_2}^{mobile} = \phi \cdot d \cdot A \cdot s_g \cdot \chi_{CO_2}^g$. Here, ϕ, d, A denote the local porosity and depth as well as the pixel area, respectively, constituting together the local pore volume, which according to assumption V can be determined accurately, cf. also SI. Fig. 4. Based on assumption I, the saturation s_g, takes the value 1 in the region of detected mobile CO_2 and 0 otherwise and is thereby fully prescribed by the phase segmentation. It remains to identify the mass concentration of CO_2 in the gaseous phase $\chi_{CO_2}^g$ which is given by the density of gaseous CO_2 under operational conditions, obtained from the NIST database (Lemmon et al.2022) Here, a uniform temperature distribution of 23 °C is assumed in the rigs; in addition, the fluid pressure is determined from local
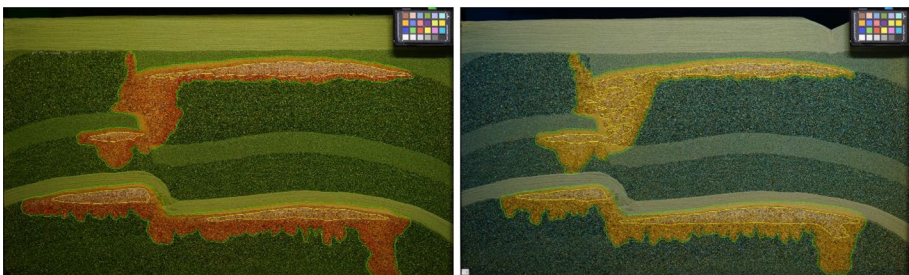

Fig. 7 Phase segmentation for the same experimental set-up under the same conditions, only differing the use of the pH-indicator mix. Left: pH-indicator mix 1 is used, and the segmentation detects gaseous regions (yellow contours) based on variations in the red color and tuned to detect dry sand. Right: pH-indicator mix 2 is used, and the segmentation detects gaseous regions (yellow contours) based on the variations in the yellow color, which are less pronounced compared to the left image. As a result, residual trapped and rising mobile CO_2 is detected in the upper zone on the right image

meteorological weather measurements, cf. SI. Fig. 2, taking into account the local height difference between the FluidFlower rigs (~29 m corresponding to increase of 3.625 mbar) and additional hydrostatic pressure of 1013.25 mbar/m from the free water level. This finally determines $m_{CO_2}^{mobile}$.

3.5 Experimental Results and Variations in CO_2 Migration Patterns

Here, we compare the 16 CO_2 injection experiments (12 in the Albus geometry, and four in the Bilbo geometry), describe the observed multi-phase flow and CO_2 migration patterns, evaluate physical reproducibility and discuss the impacts from key operational conditions, including the effect of degassed aqueous phase and different pH-indicator mixes.

3.5.1 CO_2 Migration Patterns in the Albus and Bilbo Geometries

The CO_2 migration for 10 operationally comparable CO_2 injection experiments in the Albus geometry follows a similar pattern, which is described next with reference to Fig. 8: The gaseous CO_2 injected in the *Lower F* layer (I1) quickly dissolves in the formation water and changes the color of the pH-indicator. With continued CO_2 injection, the CO_2 saturated water spreads out in a U-shape from the injection port, upwards until it reaches the *Lower seal*. At this stage both gaseous CO_2 and CO_2 saturated water are observed and distinguished. CO_2 migrates to the left, below the *Lower seal,* and accumulates in the anti-clinal fold trap (contour 1—light blue). As the gas accumulation increases in the trap, the U-shape above the injection port expands, and gravitational fingers develop under the gas accumulation when CO_2 injection in port 1 stops (contour 2—dark blue). The migration from the second CO_2 injection port (I2) is initially characterized with a small gas accumulation in the small anticlinal trap below the *Upper C* layer on the left side of the fault
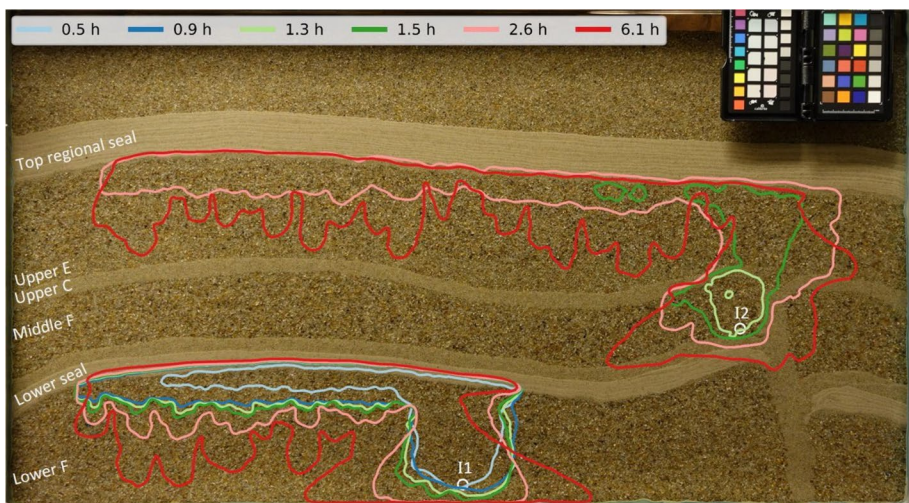

Fig. 8 The migration pattern of CO_2 in the Albus geometry during experiment AC10, representing the general pattern observed for all 10 experiments (AC01–AC10). The contours represent the distribution of gaseous and aqueous CO_2 at different times: 0.9 h represent end of first injection (I1) and 2.6 h represent end of second injection (I2)

(contour 3-light green). When the gas reaches the anticlinal trap spill point (cf. Figure 6, top), buoyancy forces cause the gas to continue through the *Upper E* layer and upwards until it reaches the *Top Regional seal* (contour 4-dark green). The gas migrates stepwise upwards under the sealing unit and sequentially fills the anticlinal trap with gas. Meanwhile, the gravitational fingers below the lower gas accumulation grow (contour 2–5); after the second injection ceased (contour 5-pink) fingers develop below the *Top Regional seal* (contour 6-red). The fingers moved laterally when reaching the *Upper C* layer, before some fingers eventually continue downwards in the *Middle F* layer below.

The CO_2 migration for four CO_2 injection experiments in the Bilbo geometry follows a similar pattern (differences will be discussed later in this section), see Fig. 9: The gaseous CO_2 injected in the *Middle F* layer (I1) migrates upwards with a U-shaped accumulation of CO_2 saturated water, similar to the Albus geometry. Both residually trapped CO_2 bubbles and CO_2 saturated water occur above the injection point, with gas migrating to the left when reaching the *Lower seal* unit (contour 1—light blue). Residually trapped gas bubbles are observed from the injector to the front of the advancing gas as it fills the anticline trap. The gas accumulation slightly exceeds the spill-point (contour 2—dark blue) before it "burst" leftwards into the smeared fault trap, a process that is repeated multiple times (see discussion in Fernø et al. 2023). Some residually trapped gas bubbles are observed in the vicinity of the smeared *Lower seal* area, and a new gas accumulation develops in the smeared fault trap when CO_2 injection in port I1 stopped (contour 3- light green). The CO_2 injection continues in the second port (I2), located in the footwall of the *Upper E* layer. A small gas accumulation is observed before the gas exceeds the spill-point below the footwall of the faulted *Middle C* layer above (contour 4—dark green). Some gas flows left of the fault plane and into the footwall of the *Upper F layer,* but most of the CO_2 migrates right and accumulates under the anticline
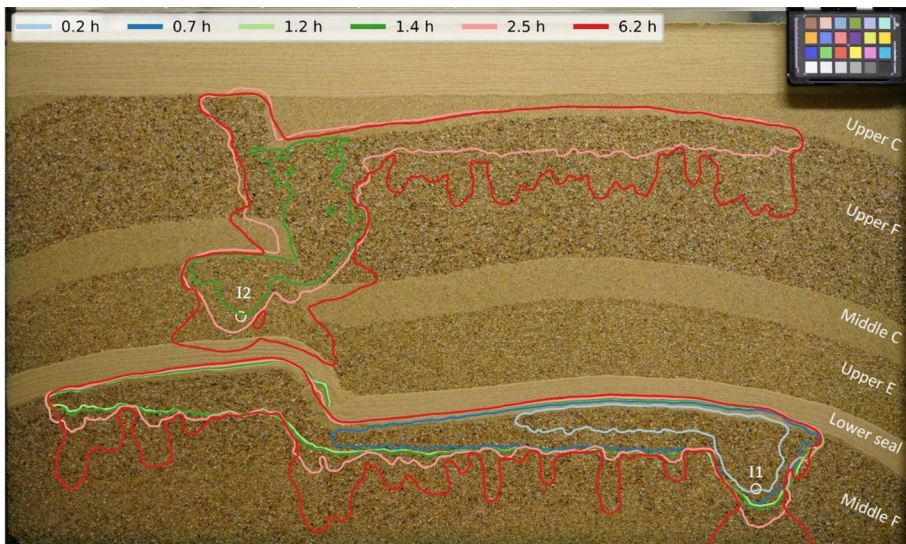

Fig. 9 The migration pattern of CO_2 during experiment BC02, representing the general pattern observed for all four (BC01-04) experiments in the Bilbo geometry. The contours represent the distribution of gaseous and aqueous CO_2 at different times: 1.2 h represent end of first injection (I1), and 2.5 h represent end of second injection (I2)

trap in the hanging wall of the *Upper F* layer. As seen in the Albus geometry, after injection has ceased in the Bilbo geometry (contour 5—pink), gravitational fingers of CO_2-saturated water develop and sink downwards (contour 6—red).

3.5.2 Quantitative Analysis of Physical Variability

To compare different experiments and assess physical variability, the phase segmentations are utilized by DarSIA to provide visualizations and convert images to data. To compute the overlap percentages, we first weight all pixels in the segmented images with their corresponding volume. Then, the ratio between the number of volume-weighted pixels where CO_2 (gaseous and dissolved) overlap is reported. The 10 repeated CO_2 injections in the Albus geometry (Fig. 10) illustrate the impact from variable degassing of the formation water. Of the 10 experiments with the same injection protocol, six experiments have pH-indicator mix 1 (Table 1). Development of calculated mass of mobile CO_2 and dissolved CO_2 over time shows a wide spread, where the effect of insufficient degassing was evident for the mobile gas at later times: with sufficient degassing, the mass of mobile CO_2 is zero for later times (AC14) because all of the injected CO_2 is dissolved in the formation water. In contrast, with insufficient degassing (atmospheric gases present in the aqueous phase) a gaseous phase remains in the geometry and is included in the mass calculations of mobile CO_2. The remaining gas at late times (observed in AC02-05 and AC08) is decreasing amounts of air, and not CO_2.

The degree of degassing influences the distribution of mobile and dissolved CO_2 in Albus geometry. Nevertheless, the overlap in spatial distribution of mobile and dissolved CO_2 for six experiments in the Albus geometry has an overall average of 65% overlapping (Fig. 11). Operational inconsistencies that reduce the overlap include (1) some CO_2 was injected in AC02 prior to starting the experiment (ramp-up), and (2) CO_2 injection was not scripted in the first experiments, causing deviation in time between CO_2 injection in port 1 and port 2 (SI. Table 1). The spatial distribution is included in supplementary information (SI. Fig. 6).
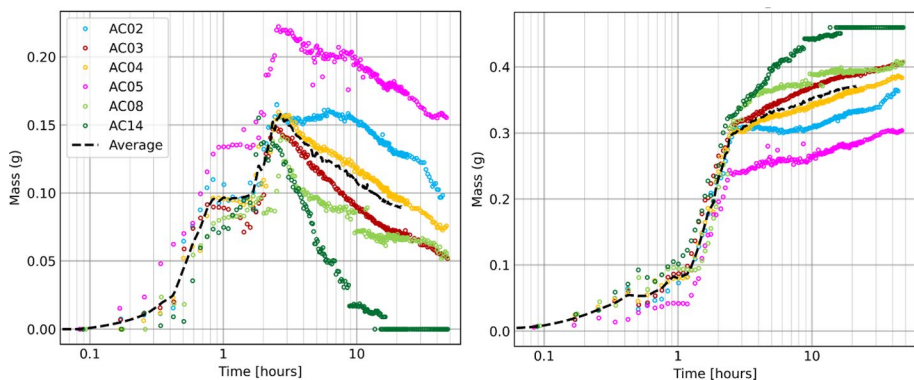

Fig. 10 Comparison of CO_2 injection experiments in the Albus geometry with the same injection protocol and pH-indicator mix. Left plot: development of calculated mass of mobile CO_2 over time, and right plot: development of calculated mass of dissolved CO_2
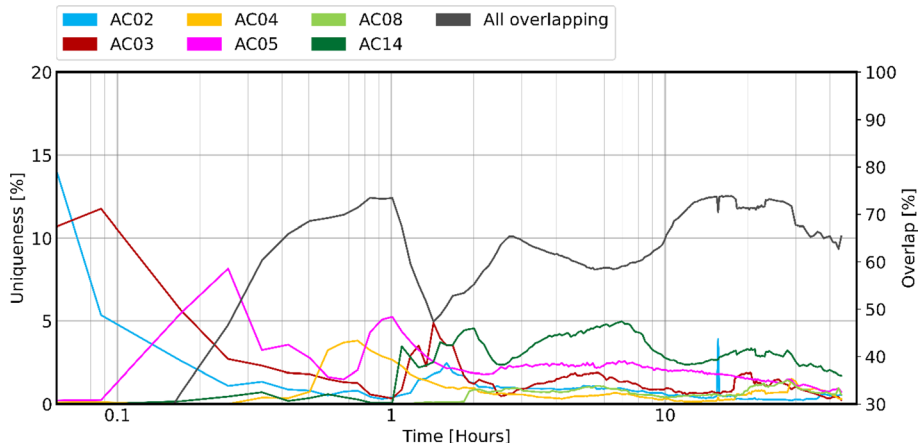
Fig. 11 Development of uniqueness of phase segmentations of dissolved CO$_2$ for six CO$_2$ injection experiments in the Albus geometry. Most of the injections have less than 5% uniqueness. The degree of overlap between all six experiments (gray, secondary y-axis) reaches a maximum (approximately 75%) after one hour, with an average of 65% for the duration of the experiments. Note that the x-axis is logarithmic

3.5.3 Impact from Different pH-Indicator Mixes

Three different pH-indicator mixes are used in the Bilbo geometry, varying in parts in their chemical properties (Table 1), as well as their interaction with the image analysis (detailed in Sect. 1.6). The development in uniqueness and overlap (Fig. 12, top) demonstrates that the experiments are comparable with less than 5% uniqueness for most of the time, where changes originate from variations in atmospheric pressure (SI. Fig. 4) or methylene red precipitation (SI. Fig. 7). The depth map of the rig (SI. Fig. 5) is also considered when computing the fractions with DarSIA, such that it really becomes volume fractions and not area fractions. Different colors are assigned to appearances of different segmentations and their overlaps (Fig. 12, bottom). Moreover, the fractions that each color represents in reference to the total covered area are calculated (and printed in the legends). As expected, the gas dissolves faster with less spreading of dissolved CO$_2$ in the BC04 experiment (pH ~ 10.4) compared to the experiments BC01– 03 (pH ~ 8.3), which is reflected in the low overlap of "BC01 + BC04" compared to "BC01 + BC03" (Fig. 12, top). Furthermore, the observation is supported by the evolution of the masses of the different CO$_2$ phases (Fig. 13). In the same figure, a clear difference between BC01 and BC03 can be observed which is directly connected to the sensitivity of the image analysis and the detection of mobile and residual trapped gaseous phase, as discussed in Sect. 1.6.

Similar material for CO$_2$ injection experiments in the Albus geometry, comparing results from pH-indicator mix 1–3 are included in supplementary information (SI. Figs. 8 and 9). To summarize, the results follow the same trends as for the CO$_2$ injection experiments in the Bilbo geometry, as presented above. We highlight the comparison of pH-indicator mix 1 and 2 (AC14 and AC09), showing an average overlap of only 81% (SI. Fig. 9), which again is attributed to the interplay of the mixes as visual markers and the image analysis. Furthermore, for the two experiments with higher degree of vacuuming of initial fluids (AC19 and AC22), an increase of the dissolution rate results in earlier attaining zero mobile/residual gas compared to the other experimental runs (SI. Fig. 8).
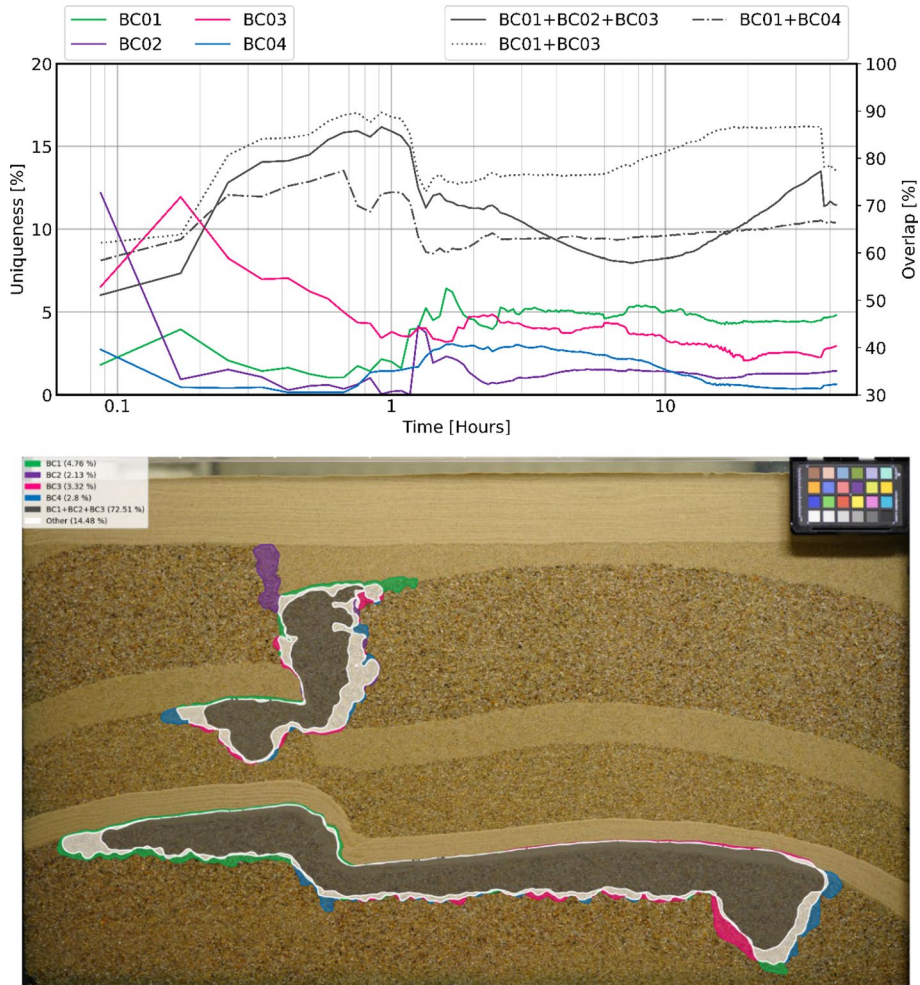
Fig. 12 The development in uniqueness and overlap for experiments BC01-04. Top: quantitative uniqueness for BC01-04 and overlap for combinations of experiments. Bottom: Spatial uniqueness after 1.5 h in BC01 (green), BC02 (purple), BC03 (pink) and BC04 (blue); overlap for BC01-03. Other overlap combinations are lumped together (white). Each color represents the spatial distribution of mobile and dissolved CO_2. Additional timesteps are shown in SI. Figure 7

4 Numerical Modeling of Experimental CO_2 Injection

Safe geologic storage of CO_2 requires numerical modeling for forecasting CO_2 migration in complex geological structures. The computational models used are typically physics-based and are expected to include all dominant processes. Nevertheless, the accuracy of these models is hard to quantify due to lack of direct observations in field conditions. The FluidFlower benchmark study (Flemisch et al. 2023) provides an insight into the accuracy of numerical models for CO_2 storage. Furthermore, Saló-Salgado et al. (2023) aim to refine our understanding of the accuracy of numerical models by systematically
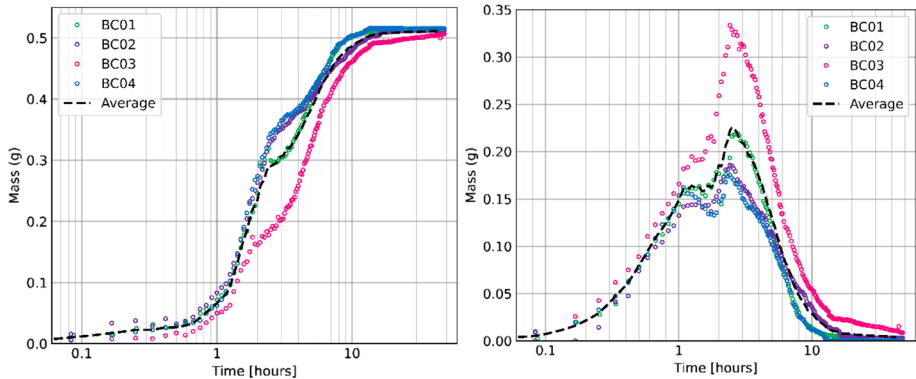
Fig. 13 Development in mass [g] of dissolved CO_2 (left) and mobile CO_2 (right) for four CO_2 injection experiments (BC01-04) in the Bilbo geometry. The overall behavior of dissolved CO_2 is comparable for all experiments, the deviation of BC03 relates to sensitivity of the image analysis with respect to threshold parameters (discussed in Sect. 2.5). Experiment with pH-indicator mix number 3 (BC04) has faster CO_2 dissolution compared to pH-indicator mix number 1 (BC01, BC02) and 2 (BC03)

evaluating the value of increasing amount of local data in predicting the CO_2 migration in FluidFlower experiments. This provides a unique opportunity to evaluate both the measurements of the petrophysical properties of the unconsolidated sand (Sect. 2.2) and CO_2 migration during injection experiments in the two studied geometries (Sect. 3).

Saló-Salgado et al. (2023) present three different versions of a numerical model (denoted Model 1 through Model 3), with, respectively, increasing amount of experimentally measured petrophysical data, while keeping all other model characteristics constant:

– Model 1 considers only grain size width as provided by the experimental measurements (Table 5) to estimate petrophysical data from published data on similar silica sand.
– Model 2 furthermore considers single-phase data from the experimental measurements, while the multiphase data remain based on published data.
– Model 3 uses all the data provided from the experimental measurements (Table 6).

To set up the simulation models, Saló-Salgado et al. (2023) complemented the experimental data made available to each model with published data to estimate the petrophysical parameters (porosity, permeability, relative permeability and capillary pressure) for each sand. History matching Models 1–3 using the AC02 experiment in the Albus geometry is detailed in Saló-Salgado et al. (2023). To history match the models, Saló-Salgado et al. (2023) used a manual iterative procedure. After a given simulation run, they quantitatively compared areas with free-phase CO_2 and water with dissolved CO_2, as well as convective finger migration times. Using the differences between estimates from experimental images and simulation values, they manually updated sand permeabilities and capillary pressure curves to be used in the next simulation run. This process required 11, 8 and 7 iterations for Model 1 to Model 3, respectively. To test the robustness of the simulation model, the petrophysical values obtained from history match in the respective Models 1–3 are used to predict migration development during CO_2 injection in the Bilbo geometry (Fig. 6), and this is detailed below.

4.1 Model Properties used for the Geometry in the Bilbo rig

4.1.1 Numerical Model Set-up

Simulation results presented here are performed with the black oil module in the MAT-LAB Reservoir Simulation Toolbox (MRST) (Lie 2019), where properties of the water are assigned to the oleic phase. Structural trapping, dissolution trapping and residual trapping (Juanes et al. 2006) are included, and details about their implementation can be found elsewhere (Saló-Salgado et al. 2023). Due to the buoyancy of CO_2 at atmospheric conditions and high permeability of the sand, very small timesteps are required for convergence of the nonlinear solver. PVT properties used in the simulations are according to atmospheric conditions (25 °C), with CO_2 in gaseous phase. The thermodynamic model is the same as applied in Saló-Salgado et al. (2023).

Dimensions of computational grid used to model the porous medium in the Bilbo rig are: $93.4 \times 53.3 \times 1.05$ cm. Layer contact coordinates are extracted from a 2D image, and our composite Pebi grid (Heinemann et al. 1991; Berge et al. 2019) has a cell size of 5 mm and a total of 20,470 cells, with a single cell layer to account for thickness and volume and obtain a 3D grid (SI. Fig. 10). The grid cell size is very similar to the one used in Saló-Salgado et al. (2023); their analysis shows that (1) this resolution is fine enough to achieve very good concordance to the AC02 experiment, and (2) model calibration is cell size dependent. There are no-flow boundary conditions everywhere except at the top surface, where there is constant pressure consistent with atmospheric pressure and a fixed-height water table. The model is initialized with 100% water saturation and hydrostatic pressure. Injection is conducted using injector wells with 1.8 mm diameter completed in a single cell at the respective coordinates (e.g. chapter 4.3.2 in Lie 2019; Fig. 6). The CO_2 injection schedule in the simulations is the same as in the Bilbo experiments (Table 3).

4.1.2 Petrophysical Input Parameters

The input values for porosity, absolute permeability and relative permeability used in the Bilbo model are identical to the ones used to match the AC02 experiment Model 1 to 3 (SI. Table 2), detailed in Saló-Salgado et al. (2023). During CO_2 injection in AC02, the sealing capacity of the C-sand was not critical due to the location of the injection ports and the injection protocol used. Hence, the calibration based on history matching this injection retains a high degree of uncertainty for the C-sand. This becomes prominent when simulating the Bilbo-geometry, where the second injection port is in the *Upper E* layer, overlayed by the faulted *Middle C* layer (Fig. 6). When the Albus AC02 HM values are used for capillary entry pressure for sand C in the Bilbo geometry, free-phase CO_2 migrates through the *Middle C* layer in the footwall instead of filling the fault trap to the spill-point. To mitigate this effect, we choose to decrease the gas saturation at which the capillary entry pressure is defined (Sge) and increase the capillary entry pressure (Pc) in the C-sand (Table 7). The increased capillary entry pressure for the vertical fault zone was also observed experimentally (see SI. Fig. 3). The Pce values in Table 7 are slightly higher than the maximum value in SI. Fig. 3 (about 7 mbar), given that a run with Pce = 7 mbar still showed entry of gaseous CO_2 in the middle C-sand. The capillary pressure curves for all other sands remain identical to the ones used to history match Model 1–3 to AC02.

Table 7 C-sand values for gas saturation where the capillary entry pressure is defined (Sge) and capillary entry pressure (Pc) obtained from history match of CO$_2$ injection experiment in the Albus geometry, compared to values needed to match the CO$_2$ injection experiment in the Bilbo geometry. All other parameters are kept the same as obtained from HM of the Albus experiment for the three models

Model	Albus HM: sand C		Bilbo HM: sand C	
	Sge	Pc [mbar]	Sge	Pc [mbar]
1	1e-3	4.6	1e-4	9.3
2	1e-3	2.6	1e-4	10.0
3	1e-3	4.5	1e-4	9.6

4.2 Simulation Results

When evaluating the simulation results there are known deviations between the set-up of the numerical simulations and the physical geometry that should be kept in mind: (1) discrepancy between the temperature value used in mass calculation from experimental results and model input, which contributes to the small difference in total injected mass (SI. Fig. 11), and (2) variations in flow cell depth, where calculations from experimental results include the depth map (SI. Fig. 5) with expansion of up to ~40%, while in the model a constant expansion of 5% is used.

A qualitative comparison of gas saturation and concentration of dissolved CO$_2$ shows that all three models provide similar, and fairly accurate, results for the CO$_2$ migration during CO$_2$ injection experiment in the Bilbo geometry (Fig. 14). The relative differences between the models appear to be comparable to the difference between the model and the experiment. However, there are subtle differences:

- After 3 h, Model 1 shows CO$_2$ in the footwall of the *Upper F* layer (top left corner in Fig. 14) equal to the experiment. However, this is due to CO$_2$ spilling out of the
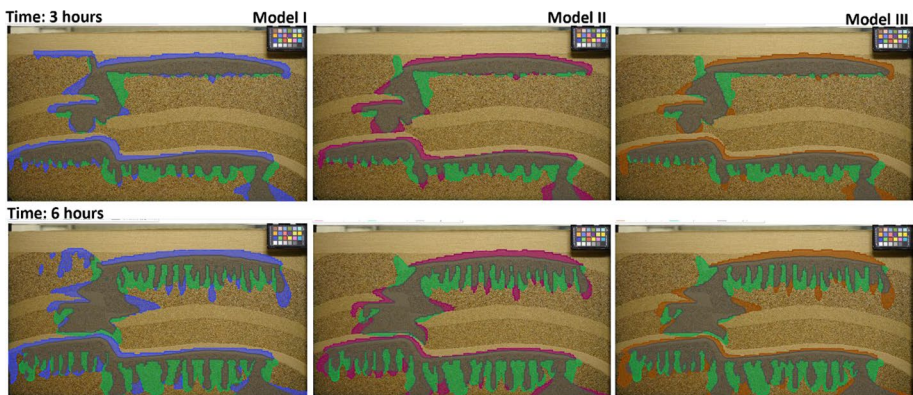

Fig. 14 Spatial uniqueness after 3 and 6 h for Model 1 (I; blue) Model 2 (II; dark pink), Model 3 (III; brown) and experiment BC01 (green); overlap between each model and experiment in gray. Each color represents the spatial distribution of mobile and dissolved CO$_2$. Contours of the simulation results are obtained from gas concentration maps, and a threshold value of 0.21 kg/m3 (15% of the maximum value around 1.4 kg/m3) is used

anticline from the right, rather than pore variability and diverging path possibilities observed experimentally.

- The models show CO_2 concentration reaching higher elevation within the middle-left and top-right C sands, with respect to the experiment.

The spatial distribution of mobile CO_2 (gas phase) and dissolved CO_2 over time (SI. Fig. 12) is quantified in Table 8, where the unique (for each case) and overlapping phase segmentations for the three Models (1, 2, 3) and experiment BC01 is compared. Note that lower uniqueness indicates better match with experiment. The distribution of mobile CO_2 for Model 2 and 3 overlaps with BC01, demonstrated as zero uniqueness for time steps in Table 8.

Quantitatively, Models 2 and 3 perform similarly and correlate better with the experimental results than Model 1, particularly regarding the amount of mobile CO_2. This is consistent with results obtained by Saló-Salgado et al. (2023) when applying the history matched models to different setting (e.g. see their Fig. 17). However, the numerical model is missing some physics compared to the experiment. An example of this is the compact sinking front with very thick and only moderately protruding fingers seen in the experiment, whereas the model shows thinner fingers sinking from a receding front, even when the diffusion coefficient is increased. We expect that this deviation between model and experiment can be reduced by incorporating hydrodynamic dispersion in the numerical model (see discussion in Saló-Salgado et al. 2023).

5 Conclusions and Future Outlook

Key learnings for constructing geological geometries (using unconsolidated sand) include: The grain sizes in adjacent layers should be close to avoid mixing as fines fall into the coarser sand; (horizontal) layers may be adjusted using a ladle in the water table using smooth movements along the whole unit length (especially important for fine-grain sand with longer settling time); faults require a minimum of one "angle tool" to depending on the fault design (with or without fault zone). For fluid injection protocol key learning includes: CO_2 injection rate should follow a scripted MFC protocol, with sufficiently high injection rate during ramp up to maintain CO_2 as a gas phase in the initial stages of injection. The development of DarSIA was important to quantify key parameters and variability in the experimentally observed CO_2 migration patterns. The results show anticipated behavior of injected CO_2, however, with physical variabilities induced by design (different formation water chemistry) and because the system is sensitive (atmospheric pressure). Numerical modeling of CO_2 injection experiments has predicted fairly accurate results for the CO_2 migration and has demonstrated the value of including measured petrophysical properties of the porous media in the simulation models. Hence, the rig represents a unique possibility to test our simulation skills because here we can compare predictions to observations.

Future outlook. The FluidFlower rig represents a fast-prototyping tool to evaluate the parameter and operational space and has been an essential part in development and planning of FluidFlower Benchmark initiative (Nordbotten et al. 2022). The presented workflows provide an excellent opportunity to address various research and particularly modeling questions. The range of possible phase configurations combined with the quick (and if needed recyclable) set-up allows for conducting a series of varying experiments

Table 8 Model-experiment comparison of the unique and overlapping spatial distribution of mobile and dissolved CO$_2$. Numbers are % of all regions with CO$_2$

Time [hours]	Mobile CO$_2$[a]					Dissolved CO$_2$[b]				
	Uniqueness				Two or more overlap	Uniqueness				Two or more overlap
	Model 1	Model 2	Model 3	BC01		Model 1	Model 2	Model 3	BC01	
3	11.4	0.0	0.0	4.3	84.2	7.4	0.9	0.8	13.9	77.0
6	28.1	0.0	0.0	0.5	71.4	6.6	1.1	1.3	19.2	71.9
9	31.2	0.0	0.0	0.2	68.6	4.1	0.9	0.7	18.4	75.9
12	38.9	0.0	0.0	0.4	60.7	3.4	0.8	0.3	17.1	78.4
18	66.8	0.0	0.0	0.0	33.2	2.8	0.4	0.2	13.4	83.2
24	71.1	0.0	0.0	0.0	28.9	2.3	0.4	0.3	11.1	85.9

[a]For simulations, gas saturation of 0.001 was used as threshold during segmentation with DarSIA

[b]For simulations, concentration of 0.21 kg/m^3 (15% of the maximum value around 1.4 kg/m^3) was used as threshold during segmentation with DarSIA (numbers from SI. Fig. 12)

and thereby performing a comprehensive physical sensitivity study, aiming at studying isolated phenomena. The access to dense observation data and a comparison with corresponding simulation data open up for better understanding and the possibility for improved modeling.

Declarations

Conflict of interest The authors have not disclosed any competing interests.

References

Beard, D.C., Weyl, P.K.: Influence of texture on porosity and permeability of unconsolidated sand. AAPG Bull. **57**(2), 349–369 (1973)

Berge, R.L., Klemetsdal, Ø.S., Lie, K.A.: Unstructured Voronoi grids conforming to lower dimensional objects. Comput. Geosci. **23**, 169–188 (2019). https://doi.org/10.1007/s10596-018-9790-0

Chapuis, R.P.: Predicting the saturated hydraulic conductivity of soils: a review. Bull. Eng. Geol. Env. **71**(3), 401–434 (2012)

Eikehaug, K., Haugen, M., Folkvord, O., Benali, B., Bang Larsen, E., Tinkova, A., Rotevatn, A., Nordbotten, J.M., Fernø, M.A.: Engineering meter-scale porous media flow experiments for quantitative studies of geological carbon sequestration. Transp. Porous Med (2024). https://doi.org/10.1007/s11242-023-02025-0

Fernø, M.A., Haugen, M., Eikehaug, K., Folkvord, O., Benali, B., Both, J.W., Storvik, E., Nixon, C.W., Gawthrope, R.L., Nordbotten, J.M.: Room-scale CO_2 injections in a physical reservoir model with faults. Transp. Porous Med (2023). https://doi.org/10.1007/s11242-023-02013-4

Flemisch, B., Nordbotten, J.M., Fernø, M.A., Juanes, R., Both, J.W., Class, H., Delshad, M., Doster, F., Ennis-King, J., Franc, J., Geiger, S., Gläser, D., Green, C., Gunning, J., Hajibeygi, H., Jackson, S.J., Jammoul, M., Karra, S., Li, J., Matthäi, S.K., Miller, T., Shao, Q., Spurin, C., Stauffer, P., Tchelepi, H., Tian, X., Viswanathan, H., Voskov, D., Wang, Y., Wapperom, M., Wheeler, M.F., Wilkins, A., Youssef, A.A., Zhang, Z.: The FluidFlower validation benchmark study for the storage of CO_2. Transp. Porous Med. (2023). https://doi.org/10.1007/s11242-023-01977-7

Folk, R.L., Ward, W.C.: Brazos river bar: a study in the significance of grain size parameter. J. Sediment. Petrol. **27**, 3–27 (1957)

Geophysical Institute, University of Bergen, https://veret.gfi.uib.no/?action=download

Glass, R.J., Conrad, S.H., Peplinski, W.: Gravity-destabilized nonwetting phase invasion in macroheterogeneous porous media: Experimental observations of invasion dynamics and scale analysis. Water Resour. Res. **36**(11), 3121–3137 (2000). https://doi.org/10.1029/2000WR900152

Heinemann, Z., Brand, C., Munka, M., Chen, Y.: Modeling reservoir geometry with irregular grids. SPE Reserv. Eng. **6**(2), 225–232 (1991). https://doi.org/10.2118/18412-PA

IEA, Net Zero by 2050. 2021: Paris

Juanes, R., Spiteri, E.J., Orr, F.M., Blunt, M.J.: Impact of relative permeability hysteresis on geological CO_2 storage. Water Resour. Res. **42**, W12418 (2006). https://doi.org/10.1029/2005WR004806

Kneafsey, T.J., Pruess, K.: Laboratory flow experiments for visualizing carbon dioxide-induced Density-Driven Brine Convection. Transp. Porous Med. **82**, 123–139 (2010). https://doi.org/10.1007/s11242-009-9482-2

Krishnamurthy, P. G., DiCarlo, D. & Meckel, T.: Geologic heterogeneity controls on trapping and migration of CO_2. Geophys. Res. Lett. 49, 1–208 (2022) https://doi.org/10.1029/2022GL099104

Krumbein, W.C.: Application of logarithmic moments to size frequency distributions of sediments. Jnl. Sed. Petrol. **6**, 35–47 (1936)

Krumbein, W.C., Monk, G.D.: Permeability as a Function of the Size Parameters of Unconsolidated Sand. Petroleum Technology (1942)

Lemmon, E.W., Bell, I.H., Huber, M.L., McLinden, M.O.: Thermophysical Properties of Fluid Systems, NIST Chemistry WebBook, NIST Standard Reference Database Number 69, Eds. P.J. Linstrom and W.G. Mallard, National Institute of Standards and Technology, Gaithersburg MD, 20899, https://doi.org/10.18434/T4D303, (retrieved September 2, 2022).

Lie, K.-A.: An introduction to reservoir simulation using MATLAB/GNU Octave: User guide for the MATLAB Reservoir Simulation Toolbox (MRST). Cambridge University Press, 2019

Nordbotten, J.M., Fernø, M.A., Flemisch, B., Juanes, R., Jørgensen, M.: Final benchmark description: fluidflower international benchmark study. Zenodo (2022). https://doi.org/10.5281/zenodo.6807102

Nordbotten, J.M., Benali, B., Both, J.W., Brattekås, B., Storvik, E., Fernø, M.A.: DarSIA: An open-source Python toolbox for two-scale image processing of dynamics in porous media. Transp. Porous Med. (2023). https://doi.org/10.1007/s11242-023-02000-9

Rasmusson, M., Fagerlund, F., Rasmusson, K., Tsang, Y., Niemi, A.: Refractive-light-transmission technique applied to density-driven convective mixing in porous media with implications for geological CO_2 storage. Water Resour. Res. **53**, 8760–8780 (2017). https://doi.org/10.1002/2017WR020730

Saló-Salgado, L., Haugen, M., Eikehaug, K., Fernø, M.A., Nordbotten, J.M., Juanes, R.: Direct comparison of numerical simulations and experiments of CO_2 injection and migration in geologic media: value of local data and forecasting capability. Transp. Porous Media (2023). https://doi.org/10.1007/s11242-023-01972-y

The Engineering ToolBox (2008). *Solubility of Gases in Water vs. Temperature*. Available at: https://www.engineeringtoolbox.com/gases-solubility-water-d_1148.html [Accessed 05.07.2023].

Trevisan, L., Pini, R., Cihan, A., Birkholzer, J.T., Zhou, Q., González-Nicolás, A., Illangasekare, T.H.: Imaging and quantification of spreading and trapping of carbon dioxide in saline aquifers using meter-scale laboratory experiments. Water Resour Res. **53**, 485–502 (2017). https://doi.org/10.1002/2016WR019749

Van De Ven, C.J.C., Mumford, K.G.: Visualization of gas dissolution following upward gas migration in porous media: Technique and implications for stray gas. Adv. Water Resour. (2018). https://doi.org/10.1016/j.advwatres.2018.02.015

Van De Ven C.J.C., Mumford, K.G.: Intermediate-scale laboratory investigation of stray gas migration impacts: transient gas flow and surface expression. Environ. Sci. Technol (2020) https://doi.org/10.1021/acs.est.0c03530

Wentworth, C.K.: A scale of grade and class terms for clastic sediments. J. Geol. **30**(5), 377–392 (1922)